Damghan University Press

Journal of Nano Simulation
journal homepage: jons.du.ac.ir

Volume 1, Issue 1, Winter 2025, 22-29
DOI: 10.22128/jons.2025.979.1005

Hypoxanthine: A DFT Investigation of Tautomerism and Nonlinear Optical Behavior

Sima Esmailpourm*, Hossein Nikoofard, Mohsen Sargolzaei

Faculty of Chemistry, Shahrood University of Technology, Shahrood, Iran

HIGHLIGHTS

- This study explores the tautomerization of hypoxanthine using the B3LYP/6-31G(d) method.
- Results show that both tautomeric forms are planar, with HX1 being more stable.
- Kinetic analysis indicates enhanced rates influenced by tunneling effects.
- Both tautomers exhibit promising nonlinear optical properties, highlighting their potential in optical applications.

GRAPHICAL ABSTRACT

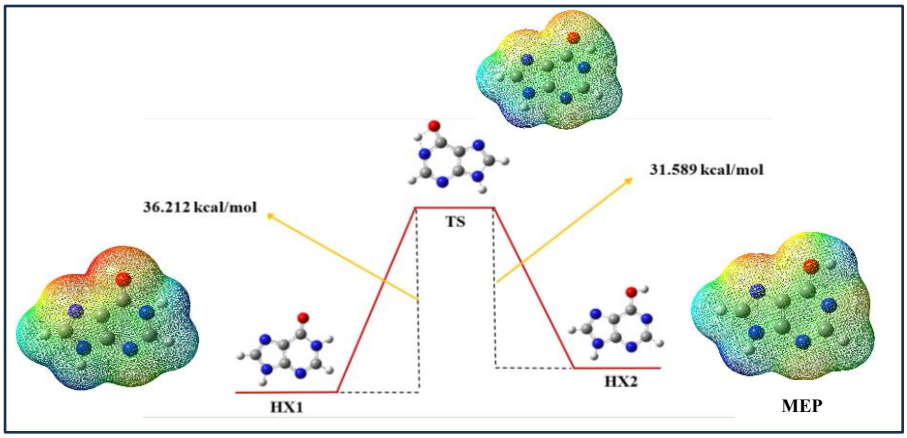

ARTICLE INFO

Article history:
Received: 2025-03-13
Received in revised form: 2025-04-22
Accepted: 2025-05-24

Available online: 2025-06-23

Keywords:
Hypoxanthine,
Hydrogen Shift,
Kinetics,
Tautomerism,
Tunneling Effect,
Wigner

ABSTRACT

This study investigates the tautomerization process of hypoxanthine using the B3LYP/6-31G(d) theoretical approach. The energy profiles derived from calculations are supplemented by kinetic rate coefficient analyses, employing transition state theory (TST). The results demonstrate that both tautomeric forms of hypoxanthine are planar, with HX1 as the more stable isomer under the studied conditions, exhibiting spontaneous and exothermic tautomerization. Kinetic analyses reveal an increased rate constant for the lactam form's formation, enhanced by tunneling effects. Transition state calculations indicate a lower energy barrier in the gas phase compared to aqueous conditions, leading to predominantly slow tautomerization rates in the absence of catalysts. Notably, both tautomers exhibit promising nonlinear optical (NLO) properties, characterized by higher hyperpolarizability relative to para-nitroaniline (pNA), even though they display lower polarizability values. Their greater dipole moments suggest potential effectiveness in NLO applications. Natural bond orbital (NBO) analysis reveals significant differences in second-order energy perturbation between HX1 and HX2, with HX1 showing reduced electron transfer from σ and π* orbitals. Additionally, the proximity of the hydroxyl group in HX2 increases perturbation energy and electron transfer, potentially contributing to the observed elongation of the C6-O10 bond length in HX1. Collectively, these tautomers represent promising candidates for further exploration in nonlinear optics.

* *Email: simaes1996@gmail.com*

1. Introduction

Hypoxanthine (1,9-Dihydro-6H-purin-6-one) is a naturally occurring purine derivative with the molecular formula $C_5H_4N_4O$ and a molecular weight of 136.11 g/mol [1, 2]. This compound is produced through the spontaneous deamination of adenine, a process that can significantly impact nucleotide metabolism and the integrity of genetic information. Due to its structural similarity to guanine, the spontaneous deamination of adenine can result in erroneous base pairing during DNA transcription and replication, as hypoxanthine pairs with cytosine instead of thymine. While guanine forms stable hydrogen bonds with cytosine, hypoxanthine's ability to mimic these bonds can lead to incorrect pairing with cytosine. Consequently, this mispairing can contribute to genetic mutations, leading to various biological repercussions [3]. In 2020, Victoria C. Yan and colleagues reported promising antiviral effects of the nucleoside analog GC-441524 against COVID-19, demonstrating superior efficacy compared to remdesivir [4]. In 2021, Ei-ichi Ami and collaborators published findings regarding the efficacy of modified nucleoside drugs in the treatment of COVID-19. Their study elucidated the mechanisms by which these modified nucleosides inhibit viral polymerases, effectively preventing viral replication [5]. In the same year, AL-Ardhi and co-authors investigated favipiravir, a nucleoside compound recognized as a broad-spectrum RNA polymerase inhibitor, as a therapeutic option for COVID-19 [6]. Given the significant antiviral potential of nucleoside and nucleotide compounds for treating COVID-19, hypoxanthine, a nucleoside analog, emerges as a promising candidate for further investigation. It is recommended that researchers conduct extensive studies to explore hypoxanthine's efficacy as a therapeutic agent against COVID-19. In the context of COVID-19, hypoxanthine has gained attention as a key compound due to its role as an intermediary metabolite in the degradation of adenosine [7].

Considering the biological significance of hypoxanthine, understanding its tautomerization behavior is crucial for the development of advanced diagnostic methods and novel therapeutic strategies. Overall, the role of hypoxanthine extends beyond its involvement in nucleotide metabolism; it also highlights the systemic effects of hypoxia and inflammation in the context of viral infections, emphasizing the intricate interplay between cellular metabolism and disease pathology. The objective of this study is to provide quantitative theoretical insights into the tautomerization reactions depicted in Scheme 1. All calculations will be conducted using Density Functional Theory (DFT), specifically utilizing the B3LYP functional [8-10], in both gas and aqueous phases. Furthermore, the kinetic rate constants will be determined at a pressure of 1 atm using Quantum Transition State Theory (QST3) [11-16] under atmospheric conditions. Additionally, the nonlinear optical (NLO) properties of these tautomeric forms will be investigated. The investigation of the nonlinear optical (NLO) properties of hypoxanthine tautomers is crucial due to the potential applications of this compound in the biomedical field. Variations in optical properties may enhance our understanding of biological mechanisms and facilitate the development of novel therapeutic strategies. In conclusion, we aim to provide qualitative chemical insights into the reaction mechanisms by examining the results obtained through donor-acceptor interaction energies and the occupancies of natural bond orbitals (NBO) [17, 18].

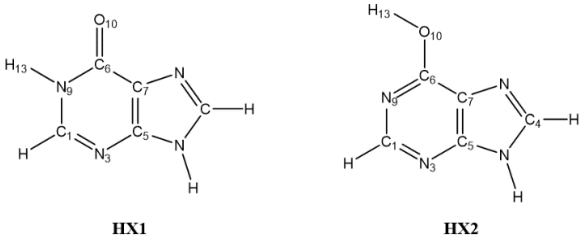

Scheme 1 The Tautomer structures of the HX.

2.Computational details

The electronic structure and energy, alongside thermodynamic calculations, were performed using the Gaussian 09 software package [19]. All geometry optimizations and harmonic vibrational frequency calculations were conducted at the B3LYP/6-31G(d) level, which is recognized as one of the optimal Density Functional Theory (DFT) functionals for thermochemistry and kinetics [8, 20-22]. The effect of the solvent on the mechanistic and thermodynamic aspects of tautomerism was investigated using a continuum model to represent the solvent environment surrounding the compounds, implemented through the Polarizable Continuum Model (PCM), with water serving as the solvent for all structures, including reactants, transition states, and products [23]. Calculations for the transition state (TS) were performed using the QST3 method at the B3LYP/6-31G(d) theoretical level. The stationary point identified as a TS structure was validated through frequency calculations, which indicated the presence of one imaginary frequency. The accuracy and reliability of the B3LYP method for studies involving hydrogen bond interactions and proton transfer have been previously assessed [24-26]. To investigate the energy profiles of the identified structures that correspond to the relevant minimum energy, intrinsic reaction coordinate (IRC) analysis was conducted in both forward and reverse directions along the reaction pathway [27, 28]. In this study, QST3 calculations were performed in conjunction with detailed IRC path analyses at the B3LYP/6-31G(d) level of theory.

3. Results and discussion

3.1. Structural characteristics of stationary points

In this section, we examine the structural properties of hypoxanthine. Based on the atom numbering in Scheme 1, several structural parameters—including bond lengths (in Å), planar angles, and dihedral angles (in degrees) for the reactants (R), transition states (TS), and products (P) of the studied reactions in both the gas phase and aqueous solvent are summarized in Table 1. The optimized structures of the tautomeric forms (lactam and lactim) of hypoxanthine are illustrated in Figure 1.

According to the values in Table 1, the bond length of C6-O10 for HX1 in the ga phase is 1.217 Å, increasing to 1.280 Å in the transition state. This increase expected and can be attributed to a decrease in bond order. The bond lengt of N9-H13 in the HX2 compound increases compared to that in the transitio state, indicating a significant structural change during the tautomeric proces This increase in bond length may be attributed to the weakening of hydroge bonds and partial charge transfer in the transition state. The data presented i Table 1 indicate that the N9-C6-C7 angle in the HX1 form is 108.08 degree which increases to 120.1 degrees in the HX2 form. This increase may b attributed to the repulsive interaction between the hydrogen atom attached t N9 and the oxygen atom O10, as corroborated by the ESP map shown in Figure 1 (as illustrated in Scheme 1). The bond angle C6-N9-C1 in the HX1 state 126.5°, while in the HX2 form, it decreases to 118.4°, indicating th compression of the six-membered ring in the HX2 state. This increase may b influenced by the repulsive interactions between N9-H and O10; howeve electronic displacement may also contribute to this effect.

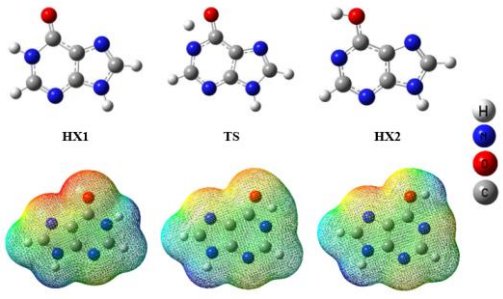

Figure 1 Optimized structures of the compound Hypoxanthine in the tautomeric forms lactam (HX1), lactim (HX2), and the transition state (TS).

Table 1 Structural parameters for all stationary points involved in the isomerization reactions, optimized at the B3LYP/6-31G(d) level of theory. (See Scheme 1 for atom labeling.)

Bond length (Å)	HX1		TS		HX2	
	Gas	Water	Gas	Water	Gas	Water
C6-O10	1.217	1.228	1.280	1.290	1.340	1.341
C6-N9	1.437	1.4205	1.373	1.3666	1.333	1.3332
N9-C1	1.365	1.365	1.344	1.345	1.346	1.347
C1-N3	1.303	1.306	1.325	1.327	1.333	1.33
N3-C5	1.362	1.361	1.348	1.349	1.337	1.339
C5-C7	1.396	1.396	1.	1.413	1.407	1.408
C7-C6	1.446	1.440	1.410	1.405	1.404	1.403
N9-H13	1.014	1.015	1.316	1.327	-	-
O10-H13	-	-	1.366	1.355	0.976	0.976
Bond angle (◦)						
N9-C6-C7	108.8	109.6	116.4	117.01	120.1	120.2
C6-N9-C1	126.5	126.2	123.7	123.43	118.5	118.4
Dihedral angle (◦)						
N9-C6-C7-O13	179.9	179.9	179.9	179.9	179.9	179.9

Table 2 Values of some thermodynamic properties of the tautomeric process of the compound HX.

Thermodynamic Properties	Reaction 1 (HX1 ↔ HX2)		Reaction 2 (HX2 ↔ HX1)	
	Gas	Water	Gas	Water
ΔE (kcal/mol)	4.497	8.236	-4.497	-8.236
ΔH (kcal/mol)	5.089	8.236	-5.089	-8.236
ΔG (kcal/mol)	4.622	8.297	-4.622	-8.297
ΔS (kcal/mol.K)	-4.19×10^{-4}	-2.02×10^{-4}	4.19×10^{-4}	2.02×10^{-4}
$\Delta E^{\dagger}$(kcal/mol)	35.937	39.612	31.440	31.376
$\Delta H^{\dagger}$(kcal/mol)	36.530	39.613	31.440	31.377
$\Delta G^{\dagger}$(kcal/mol)	36.212	39.844	31.589	31.547

The dihedral angle N9-C6-C7-O13 in the gas phase, which represents the angle of the carbonyl substituent (C=O) relative to the attached six-membered ring, is 179.9° for both tautomeric forms and the transition state of hypoxanthine. This indicates that the carbonyl substituent is planar concerning the six-membered ring, confirming that all of these structures are planar. The intrinsic reaction coordinate (IRC) pathway for the tautomerization reaction from HX1 to HX2 is illustrated in Figure 2. The IRC calculations indicate that the transition state structure connects the reactant (tautomer 1) to the product (tautomer 2).

3.2. Energetic and Thermodynamic Parameters

The parameters calculated in this study include thermodynamic properties such as enthalpy, corrected energy, Gibbs free energy, and entropy. Additionally, the activation energies for both the forward and reverse reactions within the tautomeric processes of the studied compounds have been computed. These parameters were obtained at a temperature of 298.15 K and a pressure of 1 atm, using the equations provided below.

$$\Delta M_{(E,G,H,S)} = (\varepsilon_0 + E_{corr})_{reactants} - (\varepsilon_0 + E_{corr})_{Forward} \quad (1)$$

$$\Delta M^{\dagger}_{Forward/reactaants} = (\varepsilon_0 + E_{corr})_{TS} - (\varepsilon_0 + E_{corr})_{reactants/forward} \quad (2)$$

In this section, we present properties related to the tautomeric process of hypoxanthine, including total energy (ΔE), activation energy ($\Delta E^{\dagger}$), enthalpy (ΔH), activation enthalpy of the reaction ($\Delta H^{\dagger}$), Gibbs free energy (ΔG), Gibbs activation energy ($\Delta G^{\dagger}$) expressed in kcal/mol, and entropy (ΔS) in kcal/(mol.K) for the tautomeric processes in both gas and aqueous phases, as summarized in Table 2.

The data presented in Table 2 indicate that the negative value of ΔE for the tautomeric process HX2↔HX1 in the gas phase suggests a decrease in the energy level of the molecule during the conversion from the HX2 form to the HX1 form, leading to an increase in the stability of HX1 compared to HX2. The negative enthalpy value for reaction 2 further confirms that the tautomeric reaction is exothermic. Additionally, the trend in Gibbs free energy for reaction 2 parallels that of the enthalpy, where a more negative Gibbs free energy reflects the increased stability of the HX1 compound and indicates that the reaction is spontaneous. From the energy profiles presented in Table 1, the energy barriers for the activation of the forward and reverse reactions in the gas phase are 36.212 and 31.589 kcal/mol, respectively. Thus, the tautomeric process from HX1 to HX2 is less favorable in the gas phase, while the reverse process from HX2 to HX1 is more favorable due to the lower energy barrier. These differences in activation energies and Gibbs free energies for the studied pathways indicate that the formation of isomer species 1 is kinetically favored over the formation of isomer species 2, suggesting that the production of tautomeric species 1 via reaction 2 is the most favorable reaction. The energy activation barrier diagrams for the forward and reverse reaction pathways in the gas phase are illustrated in Figure 3.

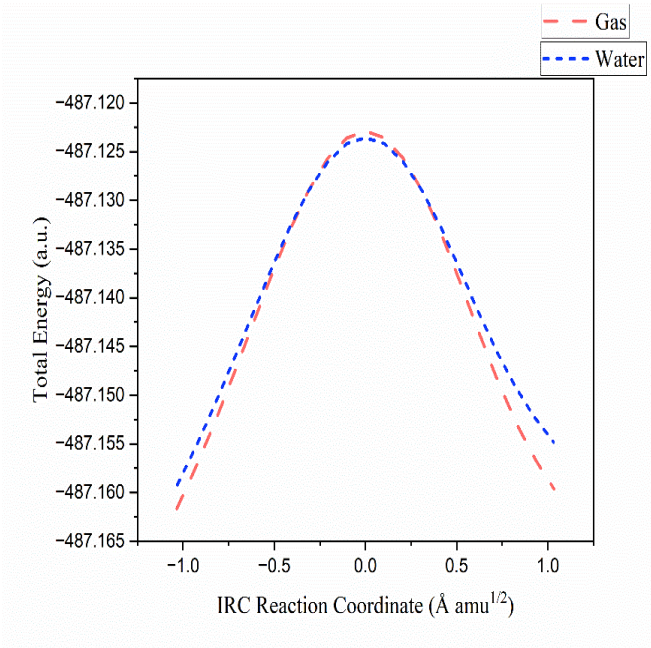

Figure 2 Intrinsic reaction coordinate (IRC) pathway for tautomerization reactions at the B3LYP/6-31G(d) level of theory in both the gas and aqueous phases.

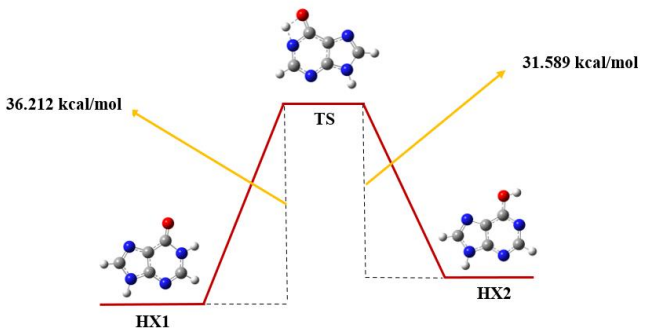

Figure 3 Activation energy barrier diagram for the tautomeric reactions [HX1 ↔ HX2] of the compound HX in the gas phase.

3.3. Kinetic parameters

One of the fundamental tools for investigating reaction mechanisms is the study of kinetics, as the reaction rate is directly dependent on the underlying mechanism and the reaction conditions. In this study, the Eyring equation (3) [29] has been employed to describe the rate constants for the forward and reverse processes of the tautomeric compounds. Furthermore, to examine the effect of tunneling on the rate constants of these reactions, the Wigner tunneling coefficient [30] was calculated using equation (4). The corrected activation energy was also determined using the Wigner tunneling coefficient, as outlined in equation (5) [29]. The obtained rate constants were subsequently adjusted using these parameters by equation (6). The relationships for the rate constants are as follows:

$$k_{T.S.T} = \frac{k_B.T}{h} e^{-\frac{\Delta G^{\dagger}}{RT}} \quad (3)$$

$$Ea_{corr} = \Delta H^{\dagger} + RT\left[1 + 2\left(\frac{w-1}{w}\right)\right] \quad (4)$$

$$Superscript w = 1 + \frac{1}{24}\left(\frac{h.c.\bar{\vartheta}_{im}}{k_B.T}\right)^2 \quad (5)$$

$$k_{corr} = w.k_{T.S.T} \quad (6)$$

In these equations, c represents the speed of light, h is Planck's constant, T denotes temperature, k_B is Boltzmann's constant, $\bar{\vartheta}_{im}$is the imaginary frequency of the transition state, and w is the Wigner tunneling coefficient. The kinetic parameters, including the rate constant ($k_{T.S.T}$) and the corrected rate constant (k_{corr}), are presented in units of s^{-1}, while the corrected activation energy (Ea_{corr}) is expressed in kcal/mol. The Wigner tunneling coefficient (w) has been calculated for the tautomeric processes of lactam and lactim in both gas and aqueous phases at a temperature of 298.15 K and a pressure of 1 atm, with the results provided in Table 3.

Table 3 Values of some kinetic properties of the tautomeric process of HX.

Parameters	Reaction 1 (HX1 ↔ HX2)	
	Gas	Water
$k_{T.S.T}$ (s^{-1})	4.214×10^{-15}	9.165×10^{-18}
w (T)	4.417	4.542
Ea_{corr} (kcal/mol)	37.728	41.129
k_{corr} (s^{-1})	1.861×10^{-14}	4.163×10^{-17}
	Reaction 2 (HX2 ↔ HX1)	
	Gas	Water
$k_{T.S.T}$ (s^{-1})	1.031×10^{-11}	1.107×10^{-11}
w (T)	4.417	4.542
Ea_{corr} (kcal/mol)	33.106	32.893
k_{corr} (s^{-1})	4.555×10^{-11}	5.032×10^{-11}

Based on the values presented in Table 1, it can be concluded that the rate constant for the tautomeric reaction pathway 2 is higher than that for pathway 1, which is associated with a decrease in the activation energy barrier (31.440 kcal/mol). Therefore, the formation of tautomer 1 occurs more readily than that of tautomer 2. The computed results indicate that both kinetic and thermodynamic perspectives favor pathway 2 over pathway 1. The Wigner tunneling coefficient is significant for correcting the activation energy and rate constant for light atoms such as hydrogen. Due to electron displacement in tautomeric processes, the rate constants for these reactions are highly sensitive to the effects of the Wigner tunneling coefficient. As demonstrated, the corrected rate constants and adjusted activation energy are indeed dependent on the Wigner tunneling.

The calculated values for the Wigner tunneling coefficient in the gas and aqueous phases are 4.417 and 4.542, respectively. Analyzing the data reveals that the corrected reaction rate has increased approximately 4.5 times after accounting for tunneling effects. Additionally, the corrected activation energy has also increased following tunneling. The significance of the Wigner tunneling coefficient for the correction of activation energy and rate constants is particularly relevant for light atoms like hydrogen, emphasizing the sensitivity of the rate constants in tautomeric reactions to tunneling effects.

3.4. NLO properties

The development of nonlinear optical (NLO) materials for various device applications requires a collaborative approach that integrates theoretical and experimental research across the fields of chemistry, physics, and engineering. Quantum chemical calculations are crucial for advancing our understanding of the electronic polarization that drives molecular NLO phenomena, as well as for defining structure-property relationships. Both polarizabilities and hyperpolarizabilities are essential parameters that describe how a system responds to an electric field. Electric polarizability is a key property of both atomic and molecular systems. These parameters not only indicate the strength of molecular interactions and influence the cross sections of diverse scattering and collision processes but also govern the NLO behavior of the system. The theory of electric polarizability is vital for elucidating a range of phenomena, including nonlinear optics, electron scattering, and effects produced by intermolecular interactions [31]. The first hyperpolarizability (β) is represented as a third-rank tensor, which can be expressed as a 3×3×3 matrix. Due to Kleinman symmetry [32, 33], the full 27 components of this three-dimensional matrix can be reduced to just 10 independent components. These components of β correspond to the coefficients in the Taylor series expansion of energy when subjected to an external electric field. Under conditions where the external electric field is both weak and homogeneous, this expansion can be expressed as:

$$E = E^0 - \mu_\alpha F_\alpha - \frac{1}{2\alpha_{\alpha\beta}F_\alpha F_\beta} - \frac{1}{6\beta_{\alpha\beta\gamma}F_\alpha F_\beta F_\gamma} + \cdots \quad (7)$$

Here E^0 denotes the energy of the non-perturbed molecules, F_α represents the electric field at the origin, while μ_α, $\alpha_{\alpha\beta}$ and $\beta_{\alpha\beta\gamma}$ are the respective components of the dipole moment, polarizability, and first hyperpolarizability. The definitions of the total static dipole moment (μ), polarizability (α), mean polarizability (α_0), and mean first hyperpolarizability (β_0) using the x, y, and z components are provided as follows [34]:

$$\mu = \left(\mu_x^2 + \mu_y^2 + \mu_z^2\right)^2 \quad (8)$$

$$\alpha = 2^{-1/2}\left[\left(\alpha_{xx} - \alpha_{yy}\right)^2 - \left(\alpha_{yy} - \alpha_{zz}\right)^2 - \left(\alpha_{zz} - \alpha_{xx}\right)^2 + 6\alpha_{xx}^2 + 6\alpha_{yy}^2 + 6\alpha_{zz}^2\right]^{1/2} \quad (9)$$

$$\alpha_0 = \frac{1}{3}\left(\alpha_{xx} + \alpha_{yy} + \alpha_{zz}\right) \quad (10)$$

$$\beta_0 = \left[\left(\beta_{xxx} + \beta_{xyy} + \beta_{xzz}\right)^2 + \left(\beta_{yyy} + \beta_{yzz} + \beta_{yxx}\right)^2 + \left(\beta_{zzz} + \beta_{zxx} + \beta_{zyy}\right)^2\right]^{1/2} \quad (11)$$

Calculations for the dipole moment, polarizability, and first hyperpolarizability were performed using the B3LYP/6-31G(d) level of theory in both gas and aqueous phases. As the values for polarizability (α_0) and hyperpolarizability (β_0) from the Gaussian 09 output are reported in atomic units (a.u.), these

Table 4 Structural parameters for all stationary points involved in the isomerization reactions, optimized at the B3LYP/6-31G(d) level of theory. (See Scheme 1 for atom labeling.)

Property	pNA	HX1		HX2	
		Gas	Water	Gas	Water
μ (Debay)	2.44 (Debye[a])	5.057	6.811	2.401	3.231
α_{xx}	-	-37.189	-33.490	-39.091	-36.034
α_{YY}	-	-66.233	-68.104	-61.864	-62.703
α_{ZZ}	-	-56.201	-56.150	-56.228	-56.229
α_0 (a.u.)	-	-53.208	-52.581	-52.394	-51.655
$\alpha_0 \times 10^{-24}$ (esu)	22.00 (cm^{3a})	-7.885	-7.793	-7.7648	-7.655
α (a.u.)	-	165.644	166.327	161.160	164.721
$\alpha \times 10^{-24}$ (esu)	-	24.548	24.650	23.884	24.412
β_{xxx}	-	-11.524	15.689	25.523	-34.111
β_{xyy}	-	-5.662	6.882	-8.794	9.3707
β_{xzz}	-	3.020	-2.833	-2.604	2.1606
β_{yyy}	-	17.702	25.724	5.138	6.4751
β_{xxy}	-	-5.662	34.49	-4.477	-4.7237
β_{yzz}	-	-2.068	-1.251	-1.97	-1.8092
β_{zzz}	-	-0.001	0.002	0.003	0.0018
β_{xxz}	-	0.004	0.003	0.021	0.0068
β_{yyz}	-	-2.068	0.001	0.007	-0.0002
β_0 (a.u.)	-	17.447	62.179	14.1859	22.580
$\beta_0 \times 10^{-33}$(esu)	15.5 (esu[a])	150.730	537.184	122.556	195.075

[a] PNA results are taken from Refs. [39-41].

Table 5 Some natural atomic charges for the two forms, HX1 and HX2, in the gas and aqueous phases.

Atoms	HX1		HX2	
	Gas	Water	Gas	Water
H13	0.441	0.460	0.501	0.516
N9	-0.634	-0.619	-0.574	-0.582
N3	-0.521	-0.533	-0.518	-0.532
C6	0.647	0.644	0.581	0.58
O10	-0.586	-0.651	-0.659	-0.677

values were converted into electrostatic units (esu) (α:1 a.u. = 0.148×10^{-24} esu and β:1 a.u. = 8.639×10^{-33}esu). p-Nitroaniline (pNA) serves as a benchmark molecule for investigating the nonlinear optical properties of molecular systems. In this research, pNA was selected due to the lack of experimental data for the compounds in question within existing literature. Various nonlinear optical compounds demonstrate significant potential for application in NLO materials, making pNA a frequently employed standard for comparison and a well-recognized example of organic NLO chromophores. Its hyperpolarizability has been examined through both experimental and theoretical approaches across different solvents and frequencies [35-38]. To determine the nonlinear optical properties of the studied compounds, values of polarizability (α), dipole moment (μ), and hyperpolarizability (β) for the compounds in both gas and aqueous phases were calculated and compared in Table 4

Urea and p-nitroaniline (pNA) were utilized as benchmarks for identifying organic candidates in nonlinear optics (NLO). Compounds with polarizability and hyperpolarizability values equal to or greater than those of the benchmark are considered suitable candidates for exhibiting NLO properties. According to the data presented in Table 4, the dipole moments of the tautomers of hypoxanthine are greater than those of pNA. Specifically, the hyperpolarizability values for HX1 and HX2 are 150.730 and 122.556, respectively, both of which exceed that of pNA. However, the polarizability values of the tautomers HX1 and HX2 are significantly lower than those of pNA. Therefore, based on the obtained results, the tautomers HX1 and HX2 exhibit promising NLO properties.

3.6. NBO properties

3.6.1 Electron Distribution and Charge Analysis

Alterations in electron distribution throughout the reaction can be analyzed by examining the atomic charges. In this context, Natural Bond Orbital (NBO) charges are particularly beneficial [42]. In Table 5, we present the NBO charges for the compounds HX1 and HX2, as well as the transition state, using the atomic numbering indicated in Scheme 1. The analysis of the NBO charges reveals that as the reaction progresses from the reactants to the transition state in reactions HX1 and HX2, the changes in partial charges are detailed in Table 5.

The data from Table 5 indicate that the atomic charge of N9 in the HX1 form is more negative than that in the HX2 form. These changes are attributed to the proton transfer from N9 to O10, resulting in a tautomeric shift that decreases the electronegativity of N9 and increases the atomic charge (greater electronegativity) at O10 in the HX2 form. In both HX1 and HX2, the atoms N9 and O10 exhibit the lowest charges within the structures, suggesting that these atoms may serve as favorable sites for electrophilic attacks due to their electron-rich nature, thus providing optimal locations for interaction with cations. According to Table 5, the atomic charge of H13 in the HX2 form is greater than that in the HX1 form, which results from the transfer of H13 away from N9 to O10. Furthermore, the positive charge on atom C6 in HX1 is greater than that in HX2. Atoms with positive charges represent optimal sites for interaction with anions; thus, these regions are susceptible to nucleophilic attacks and tend to attract electrons.

3.6.2 Natural bond orbital analysis of stationary points

Natural Bond Orbital (NBO) analysis was initially developed to quantify the contributions of resonance structures to molecular systems. The delocalization of electron density between filled (donor) Lewis-type NBOs and empty (acceptor) non-Lewis NBOs facilitates occupancy transfer from localized NBOs of the idealized Lewis structure into vacant non-Lewis orbitals. This phenomenon, referred to as the "delocalization" correction to the zero-order natural Lewis structure, results in stabilizing donor-acceptor interactions. The energies associated with these interactions can be estimated using second-order perturbation theory [17]. The delocalization energy (E^2) for each donor NBO (i) and acceptor NBO (j) is expressed as follows [43]:

$$E^2 = \Delta E_{ij} = q_i \left[\frac{F^2_{(i,j)}}{\varepsilon_i - \varepsilon_j}\right] \quad (12)$$

where ε_i and ε_j represent the diagonal matrix elements of the orbital energies, $F_{(i,j)}$ denotes the off-diagonal NBO Fock matrix elements, and q_i refers to the occupancy of the donor orbital. Table 6 presents the calculated values of second-order perturbation interaction energies, E^2, between electron donor and acceptor orbitals in the four tautomeric forms.

Table 6 Second-order perturbation energies (E^2) (in kcal/mol) for the two tautomeric forms of the compound HX.

Parameters	HX1		HX2	
	Gas	Water	Gas	Water
σ C6-N9 → σ* C1-N9	1.15	1.19	0.97	0.98
σ C6-C7 → RY* N9	0.72	0.73	0.61	0.74
σ C6-O10 → σ* C1-N9	1.39	1.47	1.99	1.97
LP(e) O10 → σ* C6-N9	1.71	1.74	6.43	6.5
σ* C6-N9 → σ* C5-C7	-	-	82.64	205.31
HOMO	-6.178	-6.269	-6.645	-6.555
LUMO	-0.857	-0.803	-0.832	-0.928
HOMO–LUMO gap (eV)	5.321	5.466	5.723	5.718

According to the data in Table 6, one notable interaction in the gas phase involves electron donation from the σ bonding orbital in C6-N9 to the σ* antibonding orbital in C1-N9, with this second-order perturbation energy being greater in the HX1 form. Conversely, the interaction energy associated with electron donation from the σ bonding orbital related to C6-O10 to the σ* antibonding orbital in C1-N9 is higher in the HX2 form. Additionally, the interaction energy involving the donation of a lone pair of electrons from atom O10 to the σ* antibonding orbital in C6-N9 is also greater in the HX2 form compared to HX1. These variations may explain the increase in the C6-O10 bond length observed in the HX1 form. Another significant interaction energy in the gas phase involves the electron donation from the π* antibonding orbital associated with C6-N9 to the π* antibonding orbital in C5-C7 in the HX2 form, which is measured at 82.64 kcal/mol. This second-order perturbation energy is absent in the HX1 form, likely due to the proximity of the hydroxyl group to the C6-N9 bond, facilitating electron transfer from C6-N9 toward C5-C7. Furthermore, with a decrease in the energy barrier, the HOMO–LUMO energy gap increases from tautomer 1 to tautomer 2. The HOMO–LUMO gaps for tautomers 1 and 2 are 5.321 eV and 5.723 eV, respectively.

3.7. Solvent effect

Using the Polarizable Continuum Model (PCM), we investigated the solvent effect on structural properties, tautomeric processes, and evaluations of Natural Bond Orbital (NBO) and Nonlinear Optical (NLO) properties. Geometric optimization calculations for the structures HX1, TS, and HX2 were conducted in an aqueous environment, with selected structural properties presented in Table 1. The analysis of the solvent effect shows that the bond lengths and dihedral angles for both tautomeric forms exhibit minimal variation in the presence of the solvent compared to the gas phase. According to the data in Table 1, water as a solvent has a negligible impact on the structural properties of these compounds. Thermodynamic properties calculated in the aqueous environment are outlined in Table 2. The results indicate that the enthalpy of the studied process increased by approximately 3 kcal/mol, while the Gibbs free energy increased by about 4 kcal/mol in the presence of water compared to the gas phase. Additionally, the activation Gibbs free energies for the forward and reverse reactions in the aqueous phase increased to 31.547 kcal/mol and 39.844 kcal/mol, respectively, relative to the gas phase, indicating that the solvent does not significantly influence the tautomeric process. The kinetic results of the tautomeric process, illustrated in Table 3, reveal that the rate constants for the forward and reverse reactions in the presence of water are 9.165×10^{-18} s^{-1} and 1.107×10^{-11} s^{-1}, respectively, showing a slight decrease compared to the gas phase.

The results regarding NLO properties indicate that the dipole moment of both tautomeric forms increases in the presence of water, suggesting enhanced polarity in the aqueous phase. Notably, the HX2 form exhibits the highest dipole moment in both phases, implying an increase in charge transfer interactions that may enhance its suitability for drug transfer or binding capabilities. While polarizability values for the tautomeric forms show minor variations in the aqueous phase compared to the gas phase, they significantly increase in the aqueous medium. We now turn to the NBO charges in the aqueous environment as detailed in Table 5. Here, we focus on the NBO charges of the atoms involved in these structures. The data from Table 5 indicate that the charges on atoms H13, N9, and N3 for both tautomeric forms increase in the presence of water compared to the gas phase. This increase in electric charge may be attributed to a reduction in the polarities of the tautomeric forms in the aqueous phase. Conversely, the electric charges on C6 and O10 for both tautomeric forms decrease in water relative to the gas phase, indicating that the polarity of these atoms is greater in the aqueous environment. Finally, the examination of the solvent effect reveals that the resonance interactions for the two studied forms do not significantly change in the presence of water compared to the gas phase. Additionally, the π*(C6-N9) → π*(C5-C7) interaction shows a significant increase in the aqueous phase, indicating enhanced resonance interactions therein.

4. *CONCLUSIONS*

A theoretical study on the lactam tautomeric form of the hypoxanthine molecule was conducted using the B3LYP/6-31G(d) computational level. The results indicate that both tautomers are planar. The thermodynamic analysis of the tautomerization processes demonstrates that the HX1 form is stable in the studied environments, with its formation being spontaneous and exothermic, reflecting the favorability of this process. Kinetic calculations of the tautomerization show an increase in the rate constant for the formation of the lactam form. Furthermore, the results reveal that the rate constant of the tautomerization reaction is sensitive to tunneling effects, which enhances the tautomerization rates for the studied compounds. Transition state calculations indicate that there is a lower energy barrier for tautomerization in the gas phase compared to the aqueous environment. Consequently, these processes are predominantly slow in the absence of a catalyst, rendering them impractical under such conditions. The study also indicates that tautomers HX1 and HX2 exhibit promising nonlinear optical (NLO) properties due to their higher hyperpolarizability values compared to para-nitroaniline (pNA). Although their polarizability values are lower than those of pNA, their greater dipole moments suggest the potential for effective interactions in NLO applications. Thus, these tautomers could be considered suitable candidates for further exploration in the field of nonlinear optics. Natural Bond Orbital (NBO) analysis shows that the second-order energy perturbation in the HX1 and HX2 forms differs significantly, with the second-order perturbation energy associated with electron transfer from σ and π* orbitals being substantially reduced in HX1. In contrast, the proximity of the hydroxyl group in HX2 leads to an increase in perturbation energy and electron transfer. These energy changes may account for the observed increase in the C6-O10 bond length in the HX1 form.

Acknowledgment

The authors wish to thank the Shahrood University of Technology for the financial support of this research work.

References:

[1] Lawal, A.T., Adeloju, S.B. Progress and recent advances in fabrication and utilization of hypoxanthine biosensors for meat and fish quality assessment: a review. *Talanta*. **2012**, 100, 217-28.

[2] Liu, L., Wang, B., Liu, D., Zou, C., Wu, P., Wang, Z., et al. Transcriptomic and metabolomic analyses reveal mechanisms of adaptation to salinity in which carbon and nitrogen metabolism is altered in sugar beet roots. *BMC plant biology*. **2020**, 20, 1-21.

[3] Lee, C.-Y.I., Delaney, J.C., Kartalou, M., Lingaraju, G.M., Maor-Shoshani, A., Essigmann, J.M., et al. Recognition and processing of a new repertoire of DNA substrates by human 3-methyladenine DNA glycosylase (AAG). *Biochemistry*. **2009**, 48, 1850-61.

[4] Yan, V.C., Muller, F.L. Advantages of the parent nucleoside GS-441524 over remdesivir for Covid-19 treatment. *ACS medicinal chemistry letters*. **2020**, 11, 1361-6.

[5] Ami, E.-I., Ohrui, H. Intriguing antiviral modified nucleosides: a retrospective view into the future treatment of COVID-19. *ACS Medicinal Chemistry Letters*. **2021**, 12, 510-7.

[6] Al-Ardhi, F.M., Novotny, L., Alhunayan, A., Al-Tannak, N.F. Comparison of remdesivir and favipiravir-the anti-Covid-19 agents mimicking purine RNA constituents. *Biomedical Papers of the Medical Faculty of Palacky University in Olomouc*. **2022**, 166.

[7] Huang, C., Wang, Y., Li, X., Ren, L., Zhao, J., Hu, Y., et al. Clinical features of patients infected with 2019 novel coronavirus in Wuhan, China. *The lancet*. **2020**, 395, 497-506.

[8] Lee, C., Yang, W., Parr, R.G. Development of the Colle-Salvetti correlation-energy formula into a functional of the electron density. *Physical review B*. **1988**, 37, 785.

[9] Becke, A.D. Density-functional thermochemistry. I. The effect of the exchange-only gradient correction. *The Journal of chemical physics*. **1992**, 96, 2155-60.

[10] Mizukami, Y. Character of frontier orbitals of antiviral drugs: candidate drugs against COVID-19. *Open Journal of Physical Chemistry*. **2020**, 10, 158.

[11] Eyring, H. The activated complex in chemical reactions. *The Journal of Chemical Physics*. **1935**, 3, 107-15.

[12] Lewis, R., Sander, S., Wagner, S., Watson, R. Temperature-dependent rate constants for the reaction of ground-state chlorine with simple alkanes. *The Journal of Physical Chemistry*. **1980**, 84, 2009-15.

[13] King, M.C., Laidler, K.J. Chemical kinetics and the radiation hypothesis. *Archive for History of Exact Sciences*. **1984**, 45-86.

[14] Connors, K.A. Chemical kinetics: the study of reaction rates in solution, Wiley-VCH Verlag GmbH, **1990**.

[15] Nikitin, E.E.e. Theory of elementary atomic and molecular processes in gases. *(No Title)*. **1974**.

[16] Smith, I.W. Kinetics and Dynamics of Elementary Gas Reactions: Butterworths Monographs in Chemistry and Chemical Engineering, Butterworth-Heinemann, **2013**.

[17] Reed, A.E., Weinstock, R.B., Weinhold, F. Natural population analysis. *The Journal of chemical physics*. **1985**, 83, 735-46.

[18] Badenhoop, J., Weinhold, F. Natural steric analysis of internal rotation barriers. *International journal of quantum chemistry*. **1999**, 72, 269-80.

[19] Frisch, M., Trucks, G., Schlegel, H., Scuseria, G., Robb, M., Cheeseman, J., et al. Gaussian09 (Wallingford, CT: Gaussian, INC.). **2009**.

[20] Becke, A.D. Density-functional thermochemistry. IV. A new dynamical correlation functional and implications for exact-exchange mixing. *The Journal of chemical physics*. **1996**, 104, 1040-6.

[21] Becke, A.D. Density-functional exchange-energy approximation with correct asymptotic behavior. *Physical review A*. **1988**, 38, 3098.

[22] Marzi, M., Shiroudi, A., Pourshamsian, K., Oliaey, A.R., Hatamjafari, F. A theoretical study of the tautomerism kinetics of 4-amino-6-methyl-3-thioxo-3, 4-dihydro-1, 2, 4-triazin-5 (2 H)-one in the gas phase: NBO population and NICS analysis. *Journal of Sulfur Chemistry*. **2019**, 40, 166-84.

[23] Barone, V., Cossi, M. Quantum calculation of molecular energies and energy gradients in solution by a conductor solvent model. *The Journal of Physical Chemistry A*. **1998**, 102, 1995-2001.

[24] Fu, A., Li, H., Du, D., Zhou, Z. Density functional study on the reaction mechanism of proton transfer in 2-pyridone: effect of hydration and self-association. *The Journal of Physical Chemistry A*. **2005**, 109, 1468-77.

[25] Novoa, J.J., Sosa, C. Evaluation of the density functional approximation on the computation of hydrogen bond interactions. *The Journal of Physical Chemistry*. **1995**, 99, 15837-45.

[26] Tayyari, S.F., Zahedi-Tabrizi, M., Rahemi, H., Mirshahi, H.A., Emampour, J., Rajabi, M., et al. A two-dimensional potential function for bent hydrogen bonded systems. II-6-hydroxy-2-formylfulvene. *Journal of Molecular Structure: THEOCHEM*. **2005**, 730, 17-21.

[27] Fukui, K. Formulation of the reaction coordinate. *The Journal of Physical Chemistry*. **1970**, 74, 4161-3.

[28] Oliaey, A.R., Shiroudi, A., Zahedi, E., Deleuze, M.S. Theoretical study on the mechanisms and kinetics of the β-elimination of 2, 2-dihaloethyltrihalosilanes (X= F, Cl, Br) compounds: a DFT study along with a natural bond orbital analysis. *Reaction Kinetics, Mechanisms and Catalysis*. **2018**, 124, 27-44.

[29] Hehre, W.J. Ab initio molecular orbital theory. *Accounts of Chemical Research*. **1976**, 9, 399-406.

[30] Wigner, E. Über das Überschreiten von Potentialschwellen bei chemischen Reaktionen. *Part I: physical chemistry. Part II: solid state physics*. **1997**, 96-109.

[31] Pir, H., Günay, N., Tamer, Ö., Avcı, D., Atalay, Y. Theoretical investigation of 5-(2-Acetoxyethyl)-6-methylpyrimidin-2, 4-dione: Conformational study, NBO and NLO analysis, molecular structure and NMR spectra. *Spectrochimica Acta Part A: Molecular and Biomolecular Spectroscopy*. **2013**, 112, 331-42.

[32] Kleinman, D.A. Nonlinear dielectric polarization in optical media. *Physical Review*. **1962**, 126, 1977.

[33] Karpagam, J., Sundaraganesan, N., Sebastian, S., Manoharan, S., Kurt, M. Molecular structure, vibrational spectroscopic, first-order hyperpolarizability and HOMO, LUMO studies of 3-hydroxy-2-naphthoic acid hydrazide. *Journal of Raman Spectroscopy: An International Journal for Original Work in all Aspects of Raman Spectroscopy, Including Higher Order Processes, and also Brillouin and Rayleigh Scattering*. **2010**, 41, 53-62.

[34] Rajamani, T., Muthu, S. Electronic absorption, vibrational spectra, non-linear optical properties, NBO analysis and thermodynamic properties of 9-[(2-hydroxyethoxy) methyl] guanine molecule by density functional method. *Solid state sciences*. **2013**, 16, 90-101.

[35] Jacob, C.R., Neugebauer, J., Jensen, L., Visscher, L. Comparison of frozen-density embedding and discrete reaction field solvent models for molecular properties. *Physical Chemistry Chemical Physics*. **2006**, 8, 2349-59.

[36] Sałek, P., Vahtras, O., Helgaker, T., Ågren, H. Density-functional theory of linear and nonlinear time-dependent molecular properties. *The Journal of chemical physics*. **2002**, 117, 9630-45.

[37] Stähelin, M., Burland, D., Rice, J. Solvent dependence of the second order hyperpolarizability in p-nitroaniline. *Chemical physics letters*. **1992**, 191, 245-50.

[38] Huyskens, F.L., Huyskens, P.L., Persoons, A.P. Solvent dependence of the first hyperpolarizability of p-nitroanilines: Differences between nonspecific dipole–dipole interactions and solute–solvent H-bonds. *The Journal of chemical physics*. **1998**, 108, 8161-71.

[39] Cheng, L.T., Tam, W., Stevenson, S.H., Meredith, G.R., Rikken, G., Marder, S.R. Experimental investigations of organic molecular nonlinear optical polarizabilities. 1. Methods and results on benzene and stilbene derivatives. *The Journal of Physical Chemistry*. **1991**, 95, 10631-43.

[40] Karna, S.P., Prasad, P.N., Dupuis, M. Nonlinear optical properties of p-nitroaniline: An ab initio time-dependent coupled perturbed Hartree–Fock study. *The Journal of chemical physics*. **1991**, 94, 1171-81.

[41] Kaatz, P., Donley, E.A., Shelton, D.P. A comparison of molecular hyperpolarizabilities from gas and liquid phase measurements. *The Journal of chemical physics*. **1998**, 108, 849-56.

[42] Márquez, E., Mora, J.R., Cordova, T., Chuchani, G. DFT calculations of triethyl and trimethyl orthoacetate elimination kinetics in the gas phase. *The Journal of Physical Chemistry A*. **2009**, 113, 2600-6.

[43] Carpenter, J., Weinhold, F. Analysis of the geometry of the hydroxymethyl radical by the “different hybrids for different spins” natural bond orbital procedure. *Journal of Molecular Structure: THEOCHEM*. **1988**, 169, 41-62.